Mechanical Properties from Periodic Plane Wave Quantum Mechanical Codes: The Challenge of the Flexible Nanoporous MIL-47(V) Framework

Danny E. P. Vanpoucke,[†,‡,§] Kurt Lejaeghere,[†,§] Veronique Van Speybroeck,[†] Michel Waroquier,[†] and An Ghysels*[,†]

[†]Center for Molecular Modeling, Ghent University, Technologiepark 903, 9052 Zwijnaarde, Belgium

[‡]Department of Inorganic and Physical Chemistry, Center for Ordered Materials, Organometallics and Catalysis (COMOC), Ghent University, Krijgslaan 281 (S3), 9000 Gent, Belgium

Ⓢ *Supporting Information*

ABSTRACT: Modeling the flexibility of metal−organic frameworks (MOFs) requires the computation of mechanical properties from first principles, e.g., for screening of materials in a database, for gaining insight into structural transformations, and for force field development. However, this paper shows that computations with periodic density functional theory are challenged by the flexibility of these materials: guidelines from experience with standard solid-state calculations cannot be simply transferred to flexible porous frameworks. Our test case, the MIL-47(V) material, has a large-pore and a narrow-pore shape. The effect of Pulay stress (cf. Pulay forces) leads to drastic errors for a simple structure optimization of the flexible MIL-47(V) material. Pulay stress is

an artificial stress that tends to lower the volume and is caused by the finite size of the plane wave basis set. We have investigated the importance of this Pulay stress, of symmetry breaking, and of *k*-point sampling on (a) the structure optimization and (b) mechanical properties such as elastic constants and bulk modulus, of both the large-pore and narrow-pore structure of MIL-47(V). We found that, in the structure optimization, Pulay effects should be avoided by using a fitting procedure, in which an equation of state $E(V)$ (EOS) is fit to a series of energy versus volume points. Manual symmetry breaking could successfully lower the energy of MIL-47(V) by distorting the vanadium−oxide distances in the vanadyl chains and by rotating the benzene linkers. For the mechanical properties, the curvature of the EOS curve was compared with the Reuss bulk modulus, derived from the elastic tensor in the harmonic approximation. Errors induced by anharmonicity, the eggbox effect, and Pulay effects propagate into the Reuss modulus. The strong coupling of the unit cell axes when the unit cell deforms expresses itself in numerical instability of the Reuss modulus. For a flexible material, it is therefore advisable to resort to the EOS fit procedure.
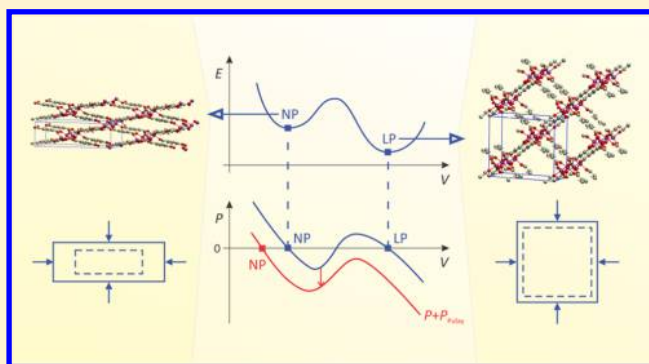
1. INTRODUCTION

Metal−organic frameworks (MOFs) present a recent class of materials which have been receiving growing interest over the past decade.[1,2] These materials show properties akin to both solids and molecular systems because they consist of inorganic metal clusters, indicated as nodes, connected through organic molecules, indicated as linkers. The linker-and-node topology often results in porous, highly tunable frameworks. Having internal surface areas of >1000 m² g⁻¹ and a chemical tunability through the choice of nodes and linkers makes MOFs versatile materials. As such, they attract much interest for application within catalysis, gas separation, and gas storage.[3−10]

This interest is clearly mirrored in the large body of experimental work on these materials and the steadily growing body of theoretical work. Due to the size and complexity of MOFs, theoretical work mostly uses force field-based methods.[5,7,9,11−15] It is very useful to be able to validate force

field findings with ab initio methods as these do not depend on the specific choices made in the force field parametrization. Over the past few years also the amount of ab initio calculations on MOFs has been growing, providing detailed insights into the fundamental physics and chemistry of these materials.[9,16−23]

A fascinating subclass of MOFs are the so-called *breathing* MOFs.[23−27] These MOFs show reversible structural phase transitions that are accompanied by large variations in unit cell volume (up to 50% and more) under the influence of thermal, mechanical, or chemical stimuli. This makes them great candidates for sensing applications. However, to build such applications, the breathing behavior needs to be thoroughly understood. Because barriers between the structural phases are
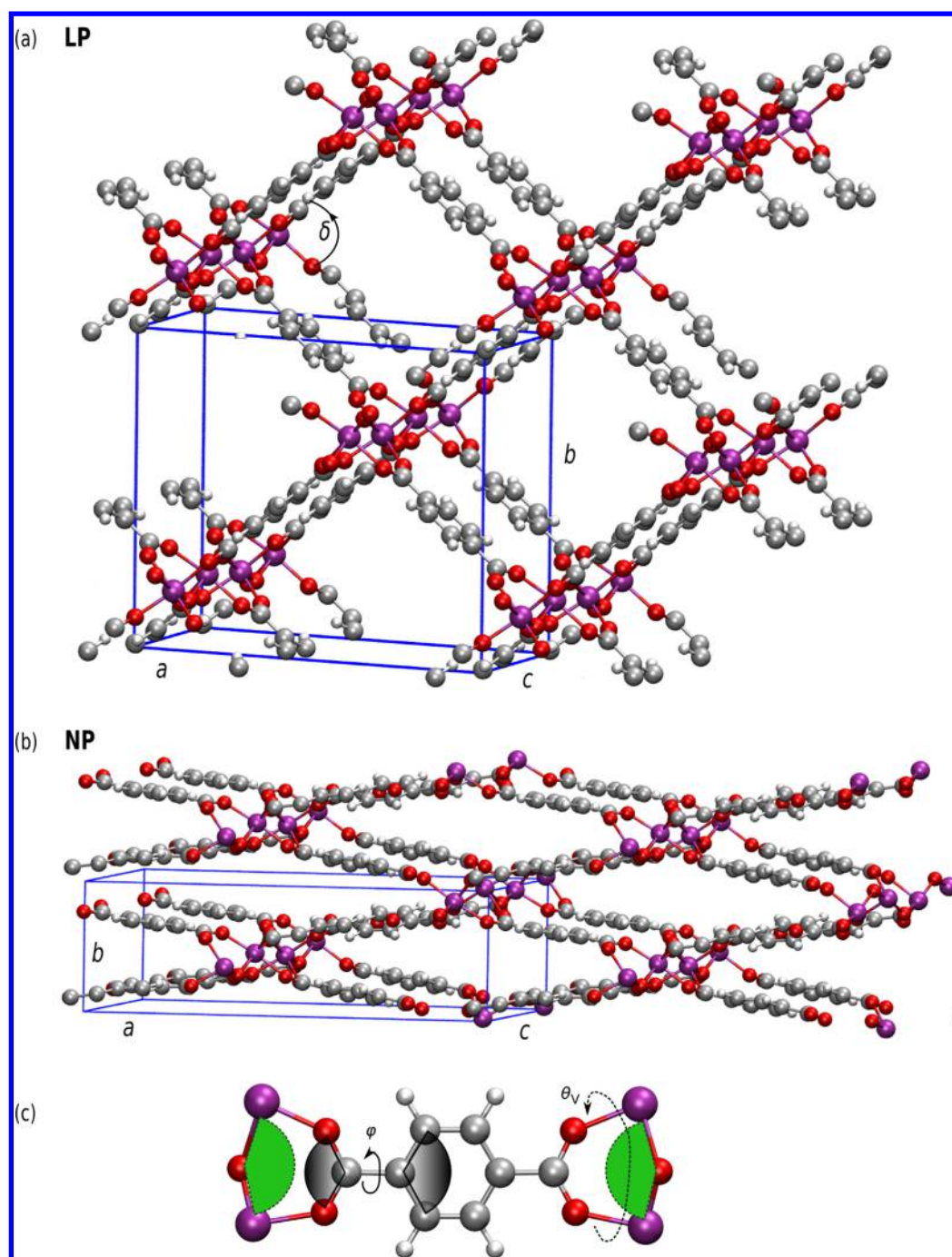
Figure 1. (a,b) Unit cell of the large-pore (LP) and narrow-pore (NP) structure of MIL-47(V), with definition of opening angle δ. (c) Definition of angles θ_V and φ. θ_V is the dihedral angle between the VCV planes of opposite vanadyl chains and is a measure for their torsion. φ is the dihedral angle between the OCO plane and the terephthalate linker and is a measure for the planarity of the linker. Color code of atoms: gray (C), red (O), white (H), and pink (V).

rather small, high-accuracy methods, such as density functional theory (DFT), are required to properly describe the energy–volume relation governing the structural phase transition.

DFT has been well established in the solid-state community for many years, and has been found to accurately handle metallic, semiconducting, and insulating materials, containing all elements of the periodic table.[28] Experience with these dense solids has, over the years, led to some general guiding rules or intuitions regarding what is required for a solid-state calculation to have a certain level of accuracy. However, in contrast to these dense compounds, MOFs represent a significantly

different class of materials. The large pores lead to very open structures and very low densities. In addition, the combination of metal(-oxide) nodes and organic linkers may lead to the emergence of low-dimensional physics.[16,20,21,23,29] Furthermore, both covalent and noncovalent interactions are essential to reproduce the equilibrium structure and thus also the unit cell. These interactions and the interplay between them are of fundamental importance to explain the breathing phenomena of some MOFs.[30−33] In the case of breathing MOFs, the structural flexibility gives rise to very flat potential energy surfaces, making structure optimization highly nontrivial.

These phenomena make it hard to find a consistent yet accurate approach to perform DFT calculations for breathing MOFs. MOFs are extended periodic frameworks; hence, DFT implementations in periodic codes are mandatory for constructing the potential energy surface accurately. A variety of studies have appeared on DFT calculations of MOFs using various computational choices. It is however not fully clear how these choices influence the overall accuracy. For instance, several authors employ a fairly sparse grid in reciprocal space of $1 \times 1 \times 1$ k-point sampling to keep MOF computations feasible.[18,34,35] Geometry optimizations are another critical point. Liu et al. optimized MIL-53 with a small k-point spacing $(0.05$ Å$^{-1})$ while keeping the unit cell parameters fixed, giving a geometry with remaining imaginary frequencies.[36] Walker et al., on the other hand, optimized MIL-53 using a $4 \times 4 \times 4$ k-grid and maintained the crystal symmetry during the optimization process.[30] Ortiz et al. published mechanical properties of several MOFs (among which MIL-47 and MIL-53) using $3 \times 3 \times 3$ k-grids.[37] Some authors already indicated problems of numerical sensitivity for porous materials. Sauer and Piccini, for instance, investigated the convergence and anharmonicity of frequency computations.[38]

In this work, we revisit guiding rules of standard solid-state computations and investigate the influence of methodological aspects with regard to the accuracy of (a) structural and (b) mechanical properties of breathing MOFs such as elastic constants and bulk moduli. Aspects of interest are real- and reciprocal-space integration grids, Pulay stresses, and symmetry.

As a case study, the MIL-47(V) MOF will be used, as shown in Figure 1a–c.[39] This MOF belongs to the subclass of breathing MOFs, where it has a somewhat special status. Unlike other breathing MOFs with the same topology (e.g., MIL-53(Al), MIL-53(Cr), ...), MIL-47(V) does not show breathing under thermal stimuli or the adsorption of gases.[25,40,41] In contrast, MIL-47(V) shows breathing under significant mechanical pressure.[23,26] Because of this more rigid nature than other breathing MOFs, MIL-47(V) is assumed to be better-behaved in the computations and thus more suitable for investigating methodological aspects.

Section 2 gives a brief introduction on standard numerical methods used in ab initio solid-state physics, while section 3 provides computational details of this work. In section 4, we study the influence of the methods and aspects discussed in section 2 on the accuracy of the structural properties in our case study of the MIL-47(V) MOF in a large-pore configuration. Guiding rules are derived for accurate calculation of the properties of breathing MOFs. These new guiding rules are then applied in section 5 to generate a narrow-pore MIL-47(V) and allow the comparison of the physical properties of the large-pore and the narrow-pore configuration. Finally, in section 6, the conclusions are presented.

2. METHODOLOGY

2.1. Solving the Schrödinger Equation for Solids.
2.1.1. Bloch Functions and k-Points. According to Bloch's theorem, the eigenfunctions of the Schrödinger equation with a periodic potential are Bloch functions, labeled by the vector $\mathbf{k}$ in reciprocal space (a k-point) and an extra index n for residual degeneracy (band index)

$$\psi_{\mathbf{k}n}(\mathbf{r}) = u_{\mathbf{k}n}(\mathbf{r}) e^{i\mathbf{k}\cdot\mathbf{r}} \tag{1}$$

where $u_{\mathbf{k}n}(\mathbf{r})$ has the same periodicity as the periodic potential. In crystalline solids, the one-electron orbitals in the Hartree–Fock or Kohn–Sham formalism need to fulfill the same type of differential equations as the Schrödinger equation and can hence be written as Bloch functions as well. Only the Bloch functions with $\mathbf{k}$ originating from a single Brillouin zone are independent, so the $\mathbf{k}$-vectors may be limited to the first Brillouin zone.

To compute the physical properties of solids, integrals over the first Brillouin zone are often required. Such integrals are in practice approximated by a sum over discrete k-points, the so-called k-point sampling. The distribution scheme by Monkhorst and Pack, for example, creates a uniformly spaced k-point grid symmetric around the Γ point and is often used.[42] Γ-point sampling considers a single Bloch function in the integral with reciprocal vector $\mathbf{k} = \mathbf{0}$ ($1 \times 1 \times 1$ sampling of the Brillouin zone), while $N \times N \times N$ sampling considers N^3 Bloch functions with $\mathbf{k}$-vectors distributed over the first Brillouin zone. Symmetry allows one to consider only the symmetry-inequivalent k-points and to write the integrals over the first Brillouin zone as a weighted sum of these irreducible k-points. The number of irreducible k-points N_{irr} hence determines the computational cost of a single self-consistent field (SCF) cycle.

2.1.2. Plane Wave Basis Set and Pulay Stress. The periodicity of the material makes the plane wave (PW) basis set $e^{i\mathbf{G}\cdot\mathbf{r}}$ a suitable choice to expand the Bloch functions. Here the reciprocal wavevectors $\mathbf{G}$ are linear combinations of the reciprocal unit cell lattice vectors $(\mathbf{G}_1,\mathbf{G}_2,\mathbf{G}_3)$. The expansion of the periodic $u_{\mathbf{k}n}(\mathbf{r})$ yields

$$\psi_{\mathbf{k}n}(\mathbf{r}) = \sum_{\mathbf{G}} u_{\mathbf{k}n,\mathbf{G}} e^{i(\mathbf{k}+\mathbf{G})\cdot\mathbf{r}} \tag{2}$$

where the coefficients $u_{\mathbf{k}n,\mathbf{G}}$ are the Fourier transform of $u_{\mathbf{k}n}(\mathbf{r})$.

In practice, numerical applications are limited to a finite PW basis set $e^{i\mathbf{G}\cdot\mathbf{r}}$. The summation over reciprocal lattice vectors in eq 2 is therefore limited to $\mathbf{G}$ vectors whose length lies below a certain cutoff G_{cut}, determined by the cutoff energy: $\hbar^2 |\mathbf{k} + \mathbf{G}|^2/(2m_e) \leq \hbar^2 G_{\text{cut}}^2/(2m_e) = E_{\text{cut}}$, for all $\mathbf{G}$. In this way, G_{cut} defines the resolution in real space as $\lambda_{\min} = 2\pi/G_{\text{cut}}$; fluctuations of $\psi_{\mathbf{k}n}(\mathbf{r})$ with shorter wavelengths are not taken into account in the basis set.

As this practical PW basis set is not complete, numerical inaccuracies appear. Even when the PW is so large that no effect can be noticed anymore in a static energy calculation, the finite size of the PW basis set still causes an artificial Pulay stress, which affects optimizations of the crystal volume. As suggested by the name, Pulay stresses are similar to Pulay forces. The latter are caused by a finite atom-centered basis set, where basis functions are attached to the position of the nucleus and are dragged along when the nucleus is displaced. If the basis set has a finite size, this creates an additional force on the nucleus, the Pulay force. Likewise, the PW basis set $e^{i\mathbf{G}\cdot\mathbf{r}}$ is linked to the unit cell dimensions through $\mathbf{G}$. When the unit cell shrinks (expands), the size of the first Brillouin zone and the corresponding reciprocal lattice vectors $\mathbf{G}$ increase (decrease). The effect is a stress toward smaller volumes.

This can be understood from Figure 2. Consider a reference volume and a PW basis set with N_{PW} plane waves, which covers a sphere in reciprocal space with a radius set by the cutoff energy E_{cut}. A volume contraction in real space corresponds to an expansion of the sphere in reciprocal space. This expansion resembles the effect of an increase in cutoff energy, i.e., as if the basis set were expanded (assuming for a moment complete k-
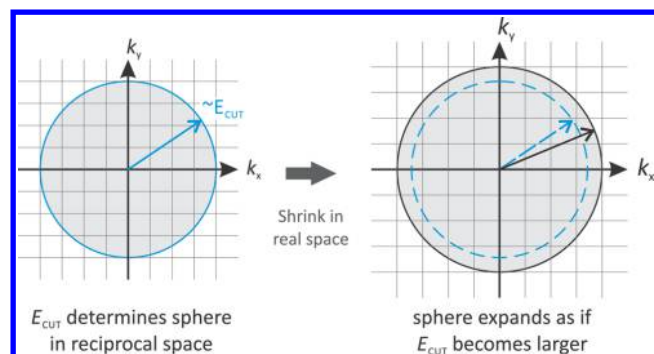
Figure 2. Cutoff energy E_{cut} determines the number of plane waves N_{PW} in the basis set, which cover a sphere in reciprocal space. Shrinking the unit cell in real space makes the sphere expand. This resembles an increase of the cutoff energy when N_{PW} is fixed, i.e., the Pulay effect.

point sampling). Because of the variational principle, this apparent basis set expansion will lower the energy. In other words, a volume contraction tends to lower the energy when the basis set is fixed. Taking a fixed finite number of plane waves N_{PW} thus creates an artificial tendency to reduce the volume in real space. This artifact is known as Pulay stress[43−46] and causes volume optimizations, which typically operate with constant basis sets, to lead to too small volumes.

2.1.3. Integration on a Real-Space Grid and Eggbox Effect. To combine both the reciprocal- and real-space parts into one set of Kohn−Sham equations, transformations between real and reciprocal space are required. In practice, this is done with a fast Fourier transform (FFT), which is an efficient implementation of the discrete Fourier transform, and which allows moving back and forth between discrete grids in real and reciprocal space. However, this may introduce numerical noise, because some high-frequency components, typically originating from the pseudopotentials and exchange-correlation potential, cannot be transformed accurately between the real-space and reciprocal-space grid, as discussed in more detail in the Supporting Information. As a result, a small displacement of all atoms with respect to the grid gives a subtle change of the wave function, energy, and forces. Only for a displacement over an entire grid spacing do these results remain invariant. Such periodic ripples as a function of the atomic shift are suitably named "eggbox effect", after the periodic layout of cardboard boxes used to transport eggs.

2.2. Structural Properties of Solids. *2.2.1. Equation of State.* One of the key structural properties of a solid is its response to volume change. The energy profile as a function of volume is constructed in the following way. First, a series of starting structures is generated by uniformly straining the unit cell vectors to impose volume increments and decrements of up to a few percent of the reference volume. Each of these starting structures should be optimized while keeping the volume fixed; the ion positions and the unit cell shape are optimized. The resulting energies are gathered as the $E(V)$ profile (energy E is expressed per unit cell).

Next, an equation of state (EOS) model $E_{EOS}(V)$ is fitted to the computed $E(V)$ curve using a least-squares criterion. The commonly used Birch−Murnaghan EOS is applicable only to moderate volume changes, because it is derived from a third-order expansion of the free energy with respect to Lagrangian strain.[47] For materials like soft MOFs, whose flexibility implies significant anharmonicity, we use the Vinet EOS, which is

known to represent compression features much better (see discussion and Figure S2 in Supporting Information).[48,49] It is based on the universal binding-energy relation for solids (UBER)[50] and depends on four material parameters: the minimum energy E_{min}, the bulk modulus B_0, the derivative of the bulk modulus with respect to pressure $B_0' = \partial B_0/\partial P$, and the volume V_{min}; all evaluated at the minimum energy point, at zero external pressure and zero temperature. If the cube root of the volume ratio V/V_{min} is denoted as $\eta = \sqrt[3]{\dfrac{V}{V_{min}}}$, the Vinet EOS reads

$$E_{EOS}(V) = E_{min} + \frac{2B_0 V_{min}}{(B_0' - 1)^2}\left[2 - (5 + 3B_0'(\eta - 1) - 3\eta)\right.$$
$$\left. \times \exp\left(-\frac{3}{2}(B_0' - 1)(\eta - 1)\right)\right] \tag{3}$$

Using such an EOS fit makes it possible not only to determine elastic properties like B_0 (see further in eq 11) but also to determine V_{min} avoiding Pulay effects.

Finally, once V_{min} is found from the fit, the corresponding unit cell shape and ion positions are determined by optimizing the ion positions and unit cell shape while keeping the volume fixed at V_{min}. This final structure will be referred to as the *EOS* structure. Its energy is denoted as $\tilde{E}_{min}$ and can slightly differ from the fit value E_{min}.

2.2.2. Γ-Point Phonons and Thermodynamical Quantities. To verify whether a geometry is a local minimum on the energy surface, a normal-mode analysis (NMA) can be performed based on the Hessian. The Hessian matrix has dimension $3N_{at} \times 3N_{at}$ (N_{at} number of atoms) and contains the second derivatives of the energy with respect to ion displacements evaluated at a stationary reference point on the energy surface[51]

$$H_{ij} = \left(\frac{\partial^2 E}{\partial x_i \partial x_j}\right)_0 \tag{4}$$

where $i,j = 1,...,3N_{at}$. NMA is equivalent with a frozen phonon calculation: the Hessian equals the dynamical matrix when the periodicity of the phonons is set to one unit cell (also called Γ-point phonons). When the Hessian is a positive semidefinite matrix and the energy gradient is zero, the structure is a local minimum on the energy surface. On the other hand, when the Hessian has n imaginary eigenvalues (frequencies), the structure is an n-fold saddle point, and a distortion of the reference geometry along the corresponding eigenvectors (normal modes) may push the structure toward a local minimum.

The phonon frequencies also serve as input in the vibrational partition function, from which several thermodynamic quantities may be derived, e.g., the zero-point energy (ZPE) and the vibrational finite-temperature corrections to the internal energy, entropy, and free energy.[52]

2.2.3. Stiffness Tensor. The stiffness tensor C is a generalization of the force constant k in Hooke's law $F = k\Delta x$ to three-dimensional solids. In the linear regime it describes the stress response to strain of the unit cell

$$\bar{\bar{\sigma}} = C \cdot \bar{\bar{\epsilon}} \tag{5}$$

where $\bar{\bar{\sigma}}$ is the Cauchy stress tensor and $\bar{\bar{\epsilon}}$ the strain tensor. We follow the definitions of the tensors as described in ref 53. In the harmonic approximation, the clamped-ion stiffness tensor

$$C_{kl}^{\text{clamp}} = \frac{1}{V_0}\left(\frac{\partial^2 E}{\partial \epsilon_k \partial \epsilon_l}\right)_0 \qquad (6)$$

is computed. It has dimension 6×6 in Voigt notation and contains the derivatives of the energy with respect to the elements of the strain tensor $\bar{\bar{\epsilon}}$, evaluated at a reference point with volume V_0, while keeping the atomic fractional coordinates fixed (hence the name clamped-ion). It can, for example, be computed by numerical differentiation of the stress tensor $\bar{\bar{\sigma}}$ at some strained structures, while keeping the fractional coordinates of the ions unaltered. An alternative method is energy-based and involves fitting the energy of strained structures to polynomials of ϵ_i, similar to how an EOS is determined, and taking the second derivative of the polynomials at the reference point.

C^{clamp} overestimates the rigidity of the material because, in reality, the ions will relax when the material is strained. The relaxed ion tensor C^{relax} is therefore computed too, by relaxing the ion positions. This can be done manually by optimizing the ion positions at each strained structure separately. It includes the anharmonicities of the ion response. Alternatively, the ion response correction can also be applied to C^{clamp} in the harmonic approximation, neglecting anharmonicities, in the following procedure. First, the "extended Hessian" with six additional rows and columns is computed. It contains the Hessian H and C^{clamp} as diagonal blocks and the force–response internal strain tensor B as off-diagonal block[53]

$$B_{i,k} = \left(\frac{\partial^2 E}{\partial x_i \partial \epsilon_k}\right)_0 \qquad (7)$$

where the mixed partial derivatives in this $3N_{\text{at}} \times 6$ matrix are evaluated at the reference structure. B is, for example, computed by numerical differentiation of either the forces in a strained cell (with constant fractional coordinates) or the stresses due to displaced ions (in a constant cell). Averaging over these two approaches can improve numerical accuracy. Next, this ionic response is added as a correction term[53] to C^{clamp}, yielding C^{relax}, denoted in short as C

$$C = C^{\text{relax}} = C^{\text{clamp}} - \frac{1}{V_0}B^T \cdot H^- \cdot B \qquad (8)$$

where H^- is the pseudoinverse of the Hessian.[53] This expression resembles the general principle of vibrational subsystem analysis (VSA), where the subsystem degrees of freedom relax adiabatically along the normal modes when the environment degrees of freedom are manipulated.[54−56] The correction term in eq 8 may be regarded as an application of VSA: the unit cell parameters are subsystem coordinates, and the ionic positions are environment coordinates. A note of caution is in order, however: the accuracy of C^{relax} is particularly sensitive to the low eigenvalues of the Hessian because of the appearance of its pseudoinverse in eq 8.

The elements of the stiffness matrix represent the resistance of the material to different deformations in different directions. On the other hand, it can also be useful to consider the eigenvalues of C. The lowest and the highest eigenvalue indicate the easiest (so-called "soft mode") and hardest deformation mode, respectively.[37,57,58]

2.2.4. Bulk Modulus. The bulk modulus describes the overall resistance to strain or stress. Several definitions exist, because volume change may be realized in several ways. Close to the reference volume, bulk moduli can be computed from the stiffness tensor, giving "harmonic" estimates. Alternatively, the bulk modulus directly relates to the second derivative of the equation of state curve $E_{\text{EOS}}(V)$, giving the EOS estimate. As noncubic unit cells are much less commonly discussed in the literature than cubic systems, we briefly revisit different measures of the bulk modulus and their interpretation.

(1) The Voigt modulus K_V is an average of the upper left corner of the stiffness tensor

$$K_V = \frac{1}{9}\sum_{i,j=1}^{3} C_{ij}$$
$$= \frac{1}{9}(C_{11} + C_{22} + C_{33} + 2C_{12} + 2C_{13} + 2C_{23}) \qquad (9)$$

It describes the average response of the linearly elastic tensile stress to isotropic volumetric strain ($\bar{\bar{\epsilon}} \to \bar{\bar{\sigma}} = C \cdot \bar{\bar{\epsilon}}$).

(2) The Reuss modulus K_R relates to the inverse of the average of the upper left corner of the compliance matrix S ($S = C^{-1}$)

$$K_R = \left(\sum_{i,j=1}^{3} S_{ij}\right)^{-1}$$
$$= (S_{11} + S_{22} + S_{33} + 2S_{12} + 2S_{13} + 2S_{23})^{-1} \qquad (10)$$

It corresponds to volume changes induced by isotropic pressure under the assumption of a linearly elastic material ($\bar{\bar{\sigma}} \to \bar{\bar{\epsilon}} = S \cdot \bar{\bar{\sigma}}$) and follows from imposing an isotropic stress tensor $\sigma_{ij} = \sigma\delta_{ij}$. The Reuss modulus may also be derived using the generalized VSA principle[56] (see discussion of eq 8) by projecting out deformation modes that keep the volume V constant. This shows that the Reuss modulus may indeed be interpreted as the response to a volume change without specifying how it is realized, allowing changes in cell shape to reduce anisotropic stresses.

(3) In the Vinet EOS, eq 3, B_0 expresses the resistance of the material against volume change and can be calculated analytically as

$$B_0 = \left(V\frac{\partial^2 E}{\partial V^2}\right)_{\text{min}} = -V_{\text{min}}\left(\frac{\partial P}{\partial V}\right)_{\text{min}} \qquad (11)$$

evaluated at the minimum-energy volume V_{min}. How the volume change is realized, e.g., by isotropic stretch or uniaxal stretch, is not specified, only that the minimum-energy geometry is taken at each volume. In the case of our ab initio calculations with periodic boundary conditions representing a single crystal, B_0 should therefore be compared with the Reuss modulus K_R.

3. COMPUTATIONAL DETAILS

Calculation of properties of MOFs with plane wave DFT is prone to numerical inaccuracies and requires extreme care to obtain reliable results. In sections 4 and 5, we demonstrate this for MIL-47(V). The starting structures are taken from the CIF database of the Cambridge Crystallographic Data Centre.[59] For the large-pore phase, we use the structure with CCDC code 846906 (dubbed "geom1"), derived from a combined experimental–theoretical study by Maurin and coauthors,[26] and the open structure (CCDC code: 166785, "geom2") measured from the empty material by the group of Férey.[39] For

Table 1. Starting Structures of MIL-47(V) for Its Large-Pore Shape (geom1 and geom2) and Narrow-Pore Shape (geom 3): Lattice Constants (Å), Lattice Angles (deg), Volume (Å³), and Symmetry

	geom1	geom2	geom3
a	16.6568	16.1433	21.117
b	13.5806	13.9392	6.710
c	6.7393	6.8179	6.717
α	90°	90°	90°
β	90°	90°	114.41°
γ	90°	90°	90°
V	1524.5	1534.2	866.7
space group	$Imma$	$Pnma$	$C2/c$
CCDC	846906	166785	846907

the narrow-pore phase, we use the closed form of Maurin and coauthors (CCDC code: 846907, "geom3").[26] Table 1 lists the cell parameters. Each unit cell contains 72 atoms in total. Energies will be expressed per unit cell.

All calculations are performed using the projector-augmented wave (PAW) method as implemented in the Vienna Ab Initio Simulation Package (VASP). For the C and O atoms, the 2s and 2p electrons are considered as valence electrons, while for the V atoms, the 3p, 3d and 4s electrons are considered as valence electrons. The exchange and correlation behavior of the electrons is modeled with the generalized gradient approximation (GGA) functional constructed by Perdew, Burke, and Ernzerhof (PBE),[60] which is known to provide reliable predictions for a wide range of solids and properties.[61] Dispersion interactions between the organic linkers are well-known to be of importance to correctly describe the MOF structure.[30,62] van der Waals interactions are modeled using the Grimme DFT-D3 corrections[63] with Becke-Johnson damping[64] and a cutoff radius of 50 Å. Spin polarization is taken into account, and the total magnetic moment per unit cell is set to 4, as every vanadium atom has one unpaired electron.

Although subsequent sections discuss the sensitivity of the results to a number of numerical parameters, there are also some common settings. First, the kinetic energy cutoff E_{cut} is set to 500 eV, corresponding to a largest wavevector $G_{cut} = 11.0$ Å^{-1}, and the criterion for energy convergence for a single SCF cycle is put at 10^{-8} eV. A Gaussian smearing scheme with a smearing factor of $\sigma = 0.05$ eV is used. The number of grid points N_{FFT} in the FFT is set to twice the number of plane waves in each direction to avoid FFT wrapping errors in reciprocal space. Finally, when optimizing the geometry, an energy convergence criterion of 10^{-7} eV is used, leading to the largest forces being only 3.2 meV/Å or less after optimization.

For phonon calculations, ionic displacements of 0.01 Å are applied, while for the determination of elastic constants, the strain tensor elements are set to 1%. The energy profile, on the other hand, is generated by changing the equilibrium volume up to ±4% in steps of 1%, to which a Vinet EOS is fitted.

4. STRUCTURE DETERMINATION OF MIL-47(V)

Because of their particular bonding character and the small energy differences involved in their structural transformations, breathing MOFs are strongly sensitive to numerical effects that do not play a significant role in other types of materials. The particular morphology of breathing MOFs gives rise to relatively flat potential energy surfaces. Different structural configurations barely differ in energy and are separated by low

energy barriers, which are prone to large inaccuracies. These structural conformations and barriers serve as input in thermodynamic models for describing the breathing behavior,[14,65] so their accurate determination is essential. In contrast, in other materials with a more coarsely shaped energy surface, the errors have less impact on the processes occurring on the potential energy surface. We will demonstrate how numerical inaccuracies may have an effect on the overall behavior of the breathing MOF. MIL-47(V) is a good prototype for this type of investigation, as it shows all features inherent to a flat energy surface as sketched above. In the following subsections the sensitivity of properties of the large-pore MIL-47(V) phase will be discussed.

Table 2. Energy Convergence with Increasing k-Point Set for Two Geometries (geom1 and geom2) and Their Difference in Energy (diff)^a

	N_{irr}		δE (meV)		
k-points	sym	nosym	geom1	geom2	diff
1 × 1 × 1	1	1	2216.7	1406.1	810.6
2 × 2 × 2	1	4	−28.1	−27.5	−0.5
3 × 3 × 3	8	14	17.8	2.0	15.8
4 × 4 × 4	8	32	0.7	−0.2	0.9
5 × 5 × 5	27	63	0.0	0.0	0.1
6 × 6 × 6	27	108	0	0	0
1 × 1 × 2	1	1	−24.4	−19.2	−5.2
2 × 2 × 4	2	8	0.9	−0.1	1.1
3 × 3 × 6	12	27	0.0	0.1	−0.1
1 × 1 × 3	2	2	44.5*	9.9	34.6
2 × 2 × 3	2	6	17.9	2.0	15.9
2 × 2 × 6	3	12	0.0	−0.1	0.2
6 × 6 × 6			E_{666}^{geom1} (eV)	E_{666}^{geom2} (eV)	diff (eV)
			−533.2859	−529.6710	3.6148

^{a}The van der Waals corrected ground-state energy E is expressed with respect to the 6 × 6 × 6 reference value: $\delta E^{geom1} = E^{geom1} - E_{666}^{geom1}$ and $\delta E^{geom2} = E^{geom2} - E_{666}^{geom2}$. For the set labeled with an asterisk, the SCF did not converge after 200 cycles. N_{irr} is the number of irreducible k-points, with symmetry turned on (sym) or off (nosym) in VASP.

4.1. Energy Convergence Test (Single Point).
In Table 2, static energy calculations are performed on the two geometries geom1 and geom2 of Table 1 as a function of the k-point set. Because our interest in the energy is mainly limited to geometry optimizations and crystal deformations, we particularly require energy differences to be well converged. When considering only $N \times N \times N$ k-grids, a 6 × 6 × 6 k-point set allows convergence up to 0.1 meV at a cost of 27 irreducible k-points, which may serve as the reference in Table 2. According to this convergence test, the Γ-point set (1 × 1 × 1) performs poorly both in absolute energy and in energy difference between geom1 and geom2, indicating that errors do not cancel out.

Because the a and b lattice vectors are longer than the c vector, we also consider some choices $N_a \times N_b \times N_c$ with $N_a = N_b < N_c$ to ensure a constant k-point density in each direction: $\Delta k \approx 2\pi/a/N_a \approx 2\pi/b/N_b \approx 2\pi/c/N_c$ ($a \approx b > c$ for MIL-47). We moreover require a very stringent convergence of energy differences (up to a few times 0.1 meV per unit cell at most), because both the large- and narrow-pore structure are separated by a small energy barrier. With six or more k-points along the shortest axis $c = 6.9$ Å, the energy is converged within 0.1 meV. Because the other lattice constants a and b are larger than c, a k-

point set of $2 \times 2 \times 6$ provides an accurate approximation of the reference $6 \times 6 \times 6$ energy at a much lower computational cost, and we therefore use this k-grid in the remainder of this work for the geometry optimization, phonon calculation, and flexibility analysis. For the interested reader, we provide computed data in the Supporting Information for the smaller k-point sets $1 \times 1 \times 1$ and $2 \times 2 \times 2$.

The eggbox effect gives energy fluctuations as a function of the real space grid position. As shown in the Supporting Information, the $2 \times 2 \times 6$ energy fluctuates by about 0.1 meV, which represents the limit of the energy accuracy.

4.2. Structure Optimization. In this discussion, structure geom1 is selected as the starting structure of the geometry optimization because it has a lower energy than geom2. A material has not only $3N_{at}$ coordinates describing the ion positions but also six coordinates ($a,b,c,\alpha,\beta,\gamma$) describing the unit cell shape and volume. These degrees of freedom can be relaxed stepwise, by first relaxing the ion positions only, then also the unit cell shape, and finally the unit cell volume as well. The effect of the relaxation on the energy is visualized in Figure 3a, and values are given in Table 3. Starting from the initial structure geom1, the *ion* geometry optimization, where only the ion coordinates are allowed to relax, lowers the energy by several tens of electronvolts. In the *shape* optimization, wherein besides the ion positions the shape of the unit cell is relaxed as well while the cell volume is kept fixed, the energy is further reduced by a few tens of millielectronvolts. In the *fully relaxed* optimization, the volume is relaxed as well, thus relaxing all $3N_{at} + 6$ degrees of freedom. We observe that in this case the MIL-47(V) structure shrinks to its NP shape. This is caused by the Pulay stress, as the optimization employs a constant yet finite basis set, pushing the structure toward smaller volumes (see below).

To avoid these Pulay effects and retrieve a local minimum for the LP phase, the EOS profile can be constructed manually. A series of structures at distinct volumes is created with a *shape* optimization (i.e., keeping the volume fixed), as described in section 2.2. Fitting the Vinet equation of state (value of four parameters available in the Supporting Information) and reoptimizing at fixed volume indeed predicts a local minimum in the LP shape at $V_{min} = 1554.1$ Å^3 and $\tilde{E}_{min} = -539.9326$ eV, which lies several millielectronvolts below the *shape* structure.

In the following, three effects are discussed that influence the geometry optimization: the above-mentioned Pulay stress, k-point sampling, and symmetry breaking. We moreover briefly discuss EOS fitting errors.

4.2.1. Pulay Stress. It is remarkable that the *fully relaxed* optimization yields a NP structure with higher energy than the *shape* optimized LP structure. This means that the conjugate gradient optimizer was able to climb a slope and overcome the barrier in the $E(V)$ profile between the LP and NP structures. The PW basis set depends on the unit cell dimensions. Following the Hellmann−Feynman theorem, the energy change due to straining the unit cell has then two components, one originating from the derivative of the Hamiltonian and another one originating from the change in basis set when the plane waves in the basis set are strained. The latter is the Pulay stress. All computed stresses are distorted by the Pulay stress, which is an artificial stress toward smaller volumes (see section 2.1). While we would normally expect that a *fully relaxed* optimization invokes a very small volume change with respect to the *shape* optimization, we observe here that MIL-47(V)
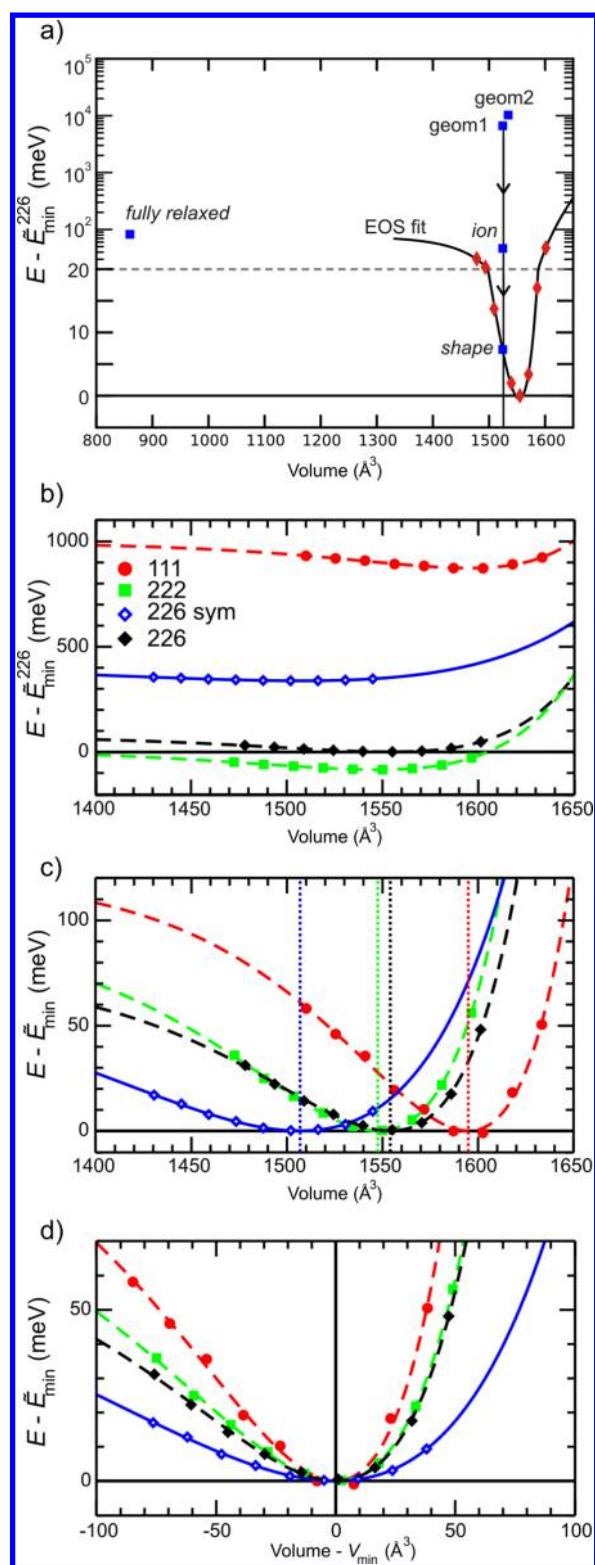

Figure 3. Structure optimization of MIL-47(V). (a) Energy and volume of the starting geometries geom1 and geom2, *ion* optimization, *shape* optimization, *fully relaxed* optimization (blue squares). The Vinet EOS is fit (black line) to a set of $E(V_i)$ points (red diamonds), see section 2.2. Energy scale is linear (bottom part) and logarithmic (top part). (b−d) The EOS is fit (lines) to a set of strained structures (symbols). Effect of Pulay stress, symmetry, and k-point sampling on the energy E_{min} (b), volume prediction V_{min} (c), and curvature B_0 (d).

Table 3. Geometry Optimizations of the LP Unit Cell, Starting from geom1[a]

	Successive Optimizations							
	k-points	δE		V	a	b	c	θ_V	φ
geom1	$2 \times 2 \times 6$	6 646.3		1524.5	16.657	13.581	6.739	0	0
ion	$2 \times 2 \times 6$	46.5	sp	1524.5	16.657	13.581	6.739	0	0
shape	$2 \times 2 \times 6$	9.7	min	1524.5	16.865	13.241	6.827	8	1−8
EOS	$2 \times 2 \times 6$	0	min	1554.1	16.394	13.854	6.842	8	1−7
Ortiz[37]	$3 \times 3 \times 3$			1524.1	16.05	13.98	6.79		

		Effects on Optimizations							
effect		k-points	δE		V	a	b	c	θ_V	φ
Pulay stress	fully relaxed	$2 \times 2 \times 6$	82.	sp	859.9	19.662	6.435	6.797	12	12
symmetry	EOS sym	$2 \times 2 \times 6$	338.	sp	1506.9	17.062	13.162	6.710	0	0
k-points	EOS	$1 \times 1 \times 1$	870.	min	1594.9	15.504	14.588	7.052	10	18−22
	EOS	$2 \times 2 \times 2$	−84.	min	1547.5	16.342	13.889	6.818	0	2
	EOS	$2 \times 2 \times 6$	0	min	1554.1	16.394	13.854	6.842	8	1−7

[a]The energy (in meV) is expressed with respect to the *EOS* energy with $2 \times 2 \times 6$ k-points: $\delta E = E - \tilde{E}_{min}^{226}$ with $\tilde{E}_{min}^{226} = -539.9326$ eV. It was verified whether the geometry is a local minimum (min) or a saddle point (sp) by computing and diagonalizing the Hessian. The volume is given per unit cell (Å³), the unit cell lengths a, b, and c (Å), the vanadyl chain angle θ_V (deg), and the benzene rotation angle φ (deg); see definition in Figure 1. Unit cell dimensions as used by Ortiz et al. in the CRYSTAL package are given for comparison.[37] The upper table displays the effects of successive optimization steps, while the lower table highlights three effects on the optimization: Pulay stress (fully relaxed), imposing symmetry, and k-point set.
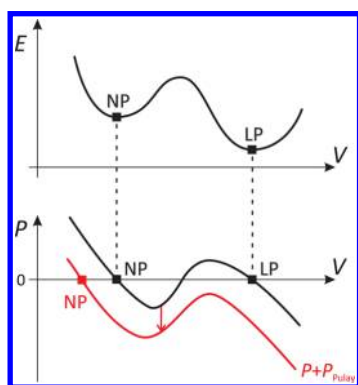

Figure 4. In a *fully relaxed* optimization, Pulay stress pushes the structure out of the LP phase toward the NP phase. The energy profile $E(V)$ has two minima and a barrier, corresponding to zeros of the pressure profile $P(V)$. Pulay stress, approximately a constant, shifts the pressure profile downward, such that the LP volume is no longer detected as a local minimum in the pressure-driven *fully relaxed* optimization.

undergoes a drastic transformation from the LP to the NP shape with a significant volume drop.

This drastic effect is visualized in Figure 4. According to the *EOS* optimization, the LP is a minimum energy structure of the $E(V)$ profile, which corresponds to a zero pressure at the LP volume. In section 5, the NP is shown to be a minimum energy structure of the $E(V)$ profile as well. The energy profile must therefore have two minima separated by a barrier, at which the pressure P is zero (see Figure 4). The *fully relaxed* optimization is driven by pressure, which is unfortunately affected by the Pulay stress. This Pulay stress, which varies only slightly as a function of volume,[46] shifts the pressure curve $P(V)$ downward, such that the apparent pressure is no longer zero at the LP structure. Pulay stress thus seems to eliminate the existence of the shallow LP minimum, pushing the system toward the NP structure.

The Pulay stress tensor is accessible by performing a stress calculation at the predicted *EOS* minimum-energy structure V_{min}, where the stress tensor should be zero in the infinite basis set limit. The deviation from zero is the Pulay stress tensor, and

in the case of LP MIL-47(V), it is found to be isotropic, lying between −0.10 and −0.14 GPa, depending on the symmetry and the used k-point set. For the *EOS* structure with a $2 \times 2 \times 6$ k-grid, the Pulay stress amounts to −0.125 GPa. This value is of the same order of magnitude as calculated transition pressures between the large- and narrow-pore phase from the literature (82−125 MPa),[23] which indeed supports the proposed mechanism shown in Figure 4.

An additional note must be made about the accuracy of the found narrow-pore structure. At first sight, the *fully relaxed* structure with a volume of 859.9 Å³ suggests that this NP shape is a second metastable state of MIL-47(V) that has not been observed experimentally under ambient conditions. However, the comparison is of limited value because of the temperature difference between calculations (at $T = 0$ K) and experiments (at finite temperature). Moreover, the *fully relaxed* optimization has been performed with the $2 \times 2 \times 6$ k-point set, which was proven to be adequate only for the description of the LP shape (Table 2). As the unit cell dimensions of the NP shape are approximately $19.7 \times 6.4 \times 6.8$ Å³, the number of two k-points along the b-axis is probably too low and needs to be enlarged. Our results based on the $2 \times 2 \times 6$ k-point set are thus not accurate enough to associate the NP shape to a local minimum or the global minimum at 0 K. This item will be further addressed in section 5.

4.2.2. k-Point Set. To highlight the sensitivity of the structure optimization to k-point sampling, the EOS profiles are constructed for the $1 \times 1 \times 1$ and $2 \times 2 \times 2$ k-point sets as well. Figure 3b confirms that the energy is not converged with these limited k-point sets, as the curves do not coincide with the reference $2 \times 2 \times 6$ k-point set. This poor performance was to be expected from our k-point convergence test in the previous subsection (Table 2). Moreover, the predicted volume deviates, as visualized in Figure 3c, and the curvature (cf. bulk modulus) of the EOS profile is not well reproduced with limited k-point sets either, as shown in Figure 3d. Apparently, one cannot rely on cancelation of errors when using too limited k-point sets in structure optimizations on such a shallow energy surface. The k-point convergence test for the energy gives a guideline for the minimal k-point set, here $2 \times 2 \times 6$, and this set should be used when doing a structure optimization as well.

Table 4. Elastic Constants for MIL-47 (in GPa): Relaxed-Ion Elastic Tensor C_{ij}, Minimum and Maximum Eigenvalue c_1 and c_6 of the C Tensor, Voigt Modulus K_V, Reuss Modulus K_R, and EOS Bulk Modulus B_0[a]

structures	k-points	C_{11}	C_{22}	C_{33}	C_{44}	C_{55}	C_{66}	C_{12}	C_{13}	C_{23}	c_1	c_6	K_V	K_R	B_0
shape	$2 \times 2 \times 6$	76.8	27.6	35.0	40.4	6.1	7.8	44.2	15.0	8.5	1.6	107.2	30.5	19.4	
EOS	$2 \times 2 \times 6$	67.6	34.0	35.4	44.2	6.7	8.7	46.0	15.2	10.2	1.8	104.7	31.1	13.6	6.1
Ortiz[37]	$3 \times 3 \times 3$	62.6	36.2	40.7	50.8	7.8	9.3	47.0	12.6	9.3	0.9	96.6	30.8	9.7	

[a]The CRYSTAL values of Ortiz et al. are included for comparison.[37]

4.2.3. Symmetry Breaking. Exploiting symmetry reduces the number of irreducible k-points from 12 to 3 when using a $2 \times 2 \times 6$ k-grid for MIL-47(V) (Table 2) and considerably lowers the computational cost of the optimization (except for the subsequent phonon calculation using finite differences, as symmetry is then broken during ion displacements). However, imposing symmetry may also lead to an incomplete scanning of the potential energy surface, overlooking lower-symmetry structures. The effect of symmetry is therefore tested by imposing the initial geom1 symmetry (*Imma*) in the $2 \times 2 \times 6$-*sym* optimization.

Imposing a symmetry constraint shifts the resulting $2 \times 2 \times 6$-*sym* EOS profile 338 meV above the reference profile (see Figure 3b and Table 3). The reason is that the symmetry constraint prevents linker rotation and vanadium chain twists from occuring during the optimization: the predicted $2 \times 2 \times 6$-*sym* EOS has all vanadiums aligned and the highest symmetry for the linkers. The structure is not a true minimum but a saddle point with some imaginary frequencies (section 2.2). Visualization of the corresponding eigenmodes indicates that these saddle point frequencies would induce a zigzag in the vanadium chain and slightly tilted linkers, thus breaking the *Imma* symmetry.

Moreover, the $2 \times 2 \times 6$-*sym* profile predicts a deviating volume in Figure 3c and deviating curvature in Figure 3d. This is an indication that linker mobility and vanadyl chain distortions should be taken into account when the prediction of accurate energy curves is the objective.

Note that allowing symmetry breaking in the optimization run not necessarily implies that the implemented geometry optimizer will break symmetry; even without imposing the initial symmetry, the structures remain highly symmetric in most cases. In our *shape* optimization, for instance, a first run gave a saddle point with imaginary frequencies representing linker rotations, despite not having constrained the symmetry. Ions were distorted manually along the lowest eigenmodes to create the starting structure of the second run, which ultimately led to a structure without any imaginary frequencies. Getting stuck in a saddle point is hard to avoid in gradient-based geometry optimizers. The force along the imaginary frequency displacement vector is zero in a saddle point, and an implementation based on symmetry will not even generate any numerical noise on this force that could make the linkers rotate, such that the starting symmetry is maintained during the whole geometry optimization.

The change in symmetry through linker rotations is observable when measuring the dihedral angles θ_V and φ (definition in Figure 1). These dihedral angles are planar in the initial structure geom1. The angles can remain zero in the optimization to a saddle point, but to find a true minimum state, these dihedral angles need to deviate slightly from zero. Moreover, not all dihedral angles in a given structure are exactly equivalent: despite the topological equivalence of linkers and V-chains, their optimized dihedral angles are not all equal,

meaning that even more symmetry has been broken. On the other hand, the unit cells in Table 3 are all orthorhombic (with deviations of less than 1°), so the symmetry of the Bravais lattice remains. Symmetry breaking through vanadyl chain distortions in the narrow-pore shape of MIL-47(V) will be discussed in section 5.

4.2.4. EOS Fitting Errors. We finally assess the influence of the quality of the Vinet fit on the EOS parameter estimations. The fit to eq 3 is performed by minimizing the root-mean-square deviation (rmsd) between the computed VASP energies $E(V_i)$ and the EOS model energies $E_{EOS}(V_i)$ at a series of volumes V_i

$$\text{rmsd} = \sqrt{\frac{\sum_{i=1}^{i=9} (E(V_i) - E_{EOS}(V_i))^2}{9}}$$

(12)

Taking into account nine volume points V_i, the rmsd is found to vary between 0.2 and 1.7 meV, depending on the number of k-points and the symmetry constraint (values in Table S3 of Supporting Information). We therefore conclude 1 meV to be a typical error on the EOS energy.

The quality of the computed energies $E(V_i)$ is affected by noise from several phenomena, such as the incompleteness of the basis set, k-grid, or internal computational routines. To estimate the effect of this noise on the four EOS parameters (V_{min}, E_{min}, B_0, and B_0' in eq 3), we apply uncorrelated random offsets to each of the energy data points $E(V_i)$, with the offsets uniformly distributed between ±1 meV. The resulting changes in the four EOS parameters are then representative for the uncertainty caused by the noise. 10^5 such data sets with random offsets are generated, and the standard deviation on each EOS parameter is taken as an estimate for the error bar. These error bars vary between ±0.3 and ±1.4 Å^3 for the equilibrium volume V_{min} and between ±0.1 and ±0.2 GPa for the bulk modulus B_0 depending on the number of k-points and the symmetry constraint (values in Table S3 of Supporting Information). Most differences in volume (see Table 3) and bulk modulus (see section 4.3) caused by varying symmetry or k-point settings are therefore significant. Symmetry and k-point convergence appear to affect the equation of state in a systematic way, changing the shape of the curve as a whole rather than randomly distorting each data point. Indeed, 1 meV error bars would be negligible on Figure 3b. Our error analysis therefore shows that differences in V_{min} and B_0 values are not due to our fitting procedure, but entirely due to the numerical convergence phenomena that are the focus of this paper.

4.3. Elastic Constants and Bulk Modulus. Table 4 compares the computed stiffness tensor for the *shape* and *EOS* structures. The elasticity tensor C has been directly obtained from the extended Hessian, using numerical differentiation of stresses and forces (eq 8). The lowest and highest eigenvalue of the stiffness tensor are listed, whose corresponding eigenvectors represent the easiest and most difficult deformation mode, respectively.[37,57,58] The Voigt modulus K_V and Reuss modulus

K_R are compared to the fitted bulk modulus B_0. All values are compared with those reported by Ortiz et al.[37]

We find the use of an *EOS*-optimized reference state to be crucial. The volume is not relaxed in the *shape* optimization, which leads to significantly different elastic constants. This means that the *shape* structure is already out of the linear elasticity regime; otherwise it would have identical elastic constants as the *EOS* structure. The *EOS* values, on the other hand, are in reasonable agreement with the values reported by Ortiz et al.,[37] despite the difference in functional and computational choices. The present work is based on the PBE functional with a $2 \times 2 \times 6$ k-point set, while the results of Ortiz et al. employ the B3LYP functional[66] with a $3 \times 3 \times 3$ k-point set in CRYSTAL09.

More disturbing is the large difference between the Reuss modulus K_R (eqs 8−10) and the fitted bulk modulus B_0 (eq 11) for the same *EOS* structure. Both K_R and B_0 represent the response of the material to isotropic stress and should in principle be identical. We posit three reasons for the discrepancy between K_R and B_0.

First, K_R is a linear response quantity, where the energy is assumed to depend quadratically on all degrees of freedom, i.e., both the ion positions and the unit cell dimensions. K_R assumes the structure to be in the linear elasticity regime and assumes harmonic ion response. The K_R value is thus the harmonic estimation, neglecting anharmonicities. In contrast, B_0 is based on the anharmonic Vinet expression $E_{EOS}(V)$, where moreover the ion positions and unit cell shape are completely relaxed at every volume point. The B_0 value thus incorporates anharmonicities.

Second, the eggbox effect can introduce some noise in the elements of the Hessian. Errors in the Hessian propagate into errors in the relaxed-ion stiffness tensor C because of eq 8, and subsequently in K_R because of eq 10. The energy oscillates with an eggbox amplitude of approximately 0.1 meV over a grid spacing of approximately 0.13 Å (see Supporting Information). This gives errors on the Hessian elements of roughly 0.5 kJ/mol/Å^2 per atom. Adding random uncorrelated uniform noise of ±0.5 kJ/mol/Å^2 to the Hessian elements gives, through eq 8, a small yet non-negligible standard deviation on the relaxed-ion stiffness tensor. For instance, the C_{11} tensor element is affected by ±0.46 GPa.

Third, the Pulay effect can affect the clamped-ion elastic constants. Errors in C^{clamp} directly propagate into errors in C because of eq 8. In our VASP calculations, the elastic constants are retrieved from a numerical differentiation of the stress tensor, which is calculated analytically for a number of deformed unit cells. These stress tensors are computed with a constant basis set. However, the desired stress tensor has a constant cutoff energy, and the difference is Pulay stress. The effect on the elastic constants is equal to the Pulay stress P_{Pulay}, as it can be regarded as evaluating the elastic constants of a material under stress. The error in C elements is thus −0.125 GPa. Moreover, the used VASP routine restarts each calculation of a deformed unit cell from the wave function of the undeformed cell without updating the PW basis set size. Although this is much more efficient than reinitializing the wave function from scratch, it will change the apparent cutoff energy, which is another undesired basis set effect.

We illustrate these Pulay effects with the C_{11}^{clamp} element, which is not affected by anharmonicities of the ions as the ions are not relaxed. The *EOS* reference structure is strained in the [100] direction by ±1%. In the energy-based approach, a parabola is fit through the three energies, and its curvature gives 98.4 GPa. This approach is free from any Pulay effect. Next, the stress tensor is constructed at every strained structure while reinitializing the wave function in order to update the basis set between these strained structures. Its numerical differentiation gives a value of 98.3 GPa. This value is affected by only the Pulay stress, which indeed explains the difference of about 0.1 GPa. Finally, the stress tensor is constructed at every strained structure without reinitializing the wave function, to simulate the VASP routine. A value of 100.1 GPa is found, which incorporates both Pulay stress and other basis set effects due to the change in apparent cutoff energy between the strained structures. In conclusion, the error in the C_{11}^{clamp} element is of the order of 2 GPa.

Unfortunately, numerical inaccuracies in Hessian and stiffness tensor elements are enhanced because of numerical instabilities in the calculation of the Reuss modulus. K_R involves both a pseudoinverse of the Hessian to compute the relaxed-ion stiffness tensor C (eq 8) as well as the inversion of C to construct the compliance tensor S (eq 10). For the particular case of MIL-47(V), the inversion of C is numerically very sensitive. Indeed, the condition number (the ratio c_6/c_1 of the highest/lowest eigenvalues of C) amounts to fairly high values of 57 and 176 for our $2 \times 2 \times 6$ EOS structure and for the structure of Ortiz, respectively. The Pulay effects of the order of 2 GPa then make all the difference: lowering only the C_{11} element by 2 GPa (3%), for example, yields a decrease in K_R of 19%. In comparison, it yields a decrease in K_V of only 0.7%, because the Voigt modulus does not require the inversion of C and is therefore fairly insensitive to errors in C. The physical origin of the numerical instability of K_R is specific to the flexible framework MIL-47(V): it is due to the strong coupling between the a and b directions.

On the basis of this analysis of the stiffness tensor, we conclude that numerical differentiation of stresses at deformed unit cells is not suitable for determining the compliance tensor or the Reuss modulus of breathing MOFs, even if it is a cheap and easy to implement methodology. It suffers from Pulay effects which are enhanced dramatically because of the coupling between the unit cell axes. Numerical differentiation of energies to construct C can limit Pulay effects. When aiming for single-crystal values, and as long as computational resources permit, we advise constructing a series of $E(V_i)$ points and fitting an equation of state, as we regard the fitted bulk modulus B_0 to be the least error prone; in addition, B_0 takes care of anharmonicities of the ions.

5. LARGE PORE VERSUS NARROW PORE OF MIL-47(V)

5.1. Structure Comparison. The MIL-47(V) MOF is a special case in the family of breathing MOFs. In contrast to other members of this family (e.g., MIL-53(Al)), it shows breathing behavior only under the application of a significant external pressure.[23,26] Using the insights and methodology developed in the previous sections, the narrow-pore (NP) version of the MIL-47(V) will now be investigated (Figure 1b). As initial geometry, we start from the structure provided in the literature[26] with lattice parameters presented in Table 1 (geom3), showing an almost 50% reduction in unit cell volume. A k-point convergence test for this structure yields results comparable to those observed for the large-pore MIL-47(V) (see Supporting Information). A Γ-centered $2 \times 6 \times 6$ k-point set corresponds to 40 irreducible k-points and offers a trade-off between accuracy and computational cost.

Table 5. Comparison of the LP (2 × 2 × 6 k-Points) and NP (2 × 6× 6 k-Points) Structures of MIL-47(V)[a]

	(1) Vinet EOS Fit Parameters				
	$\tilde{E}_{min}$ [meV]	V_{min} [Å³]	B_0 [GPa]	B' [−]	rmsd [meV]
LP	−539 932.6 (±0.3)	1554.1 (±0.6)	6.09 (±0.12)	−55.0 (±2.1)	0.472
NP	−539 918.8 (±0.3)	904.8 (±1.4)	2.84 (±0.18)	15.9 (±10.1)	0.046
LP-NP	−13.8 (±0.6)				

	(2) Structural Parameters									
	a [Å]	b [Å]	c [Å]	β [deg]	δ [deg]	r_{VO}^{long} [Å]	r_{VO}^{short} [Å]	τ [deg]	σ [deg]	b_{VV} [Å]
LP	16.394	13.854	6.842	90.19	80	2.08	1.66	175.	133.	0.31
NP	21.115	6.840	6.776	112.39	38	2.06	1.67	171.	133.	0.43

	(3) Elastic Constants and Bulk Modulus [GPa]									
	C_{11}	C_{22}	C_{33}	C_{44}	C_{55}	C_{66}	C_{12}	C_{13}	C_{23}	K_V	K_R
LP	67.6	34.0	35.4	44.2	6.7	8.7	46.0	15.2	10.2	31.1	13.6
NP	198.6	6.4	41.4	7.3	1.7	20.6	12.3	37.6	3.5	39.2	5.7

	(4) Thermal Contributions at 300 K						
	ZPE [meV]	E_{vib} [meV]	TS_{vib} [meV]	F_{vib} [meV]	F [meV]	F [kJ/mol]	$C_{V,vib}$ [meV/K]
LP	12 050.	13 347.	2 502.	10 845.	−529 088.		8.164
NP	12 073.	13 340.	2 366.	10 974.	−528 945.		8.152
LP-NP	−23.	7.	136.	−129.	−142.	−13.3	0.012

[a](1) Different parameters of the Vinet EOS (eq 3) are tabulated with the error bars assuming a noise of ±1 meV. The rmsd of the fit is also given (eq 12). (2) Structural parameters of the two structures: lattice parameters a, b, and c; lattice angle β (the two other lattice angles $\alpha = \gamma = 90.0°$) ; opening angle δ of the pore; vanadium−oxide bond lengths r_{VO}^{long} and r_{VO}^{short} along the vanadyl chain; octahedral backbone angle τ; superexchange angle σ; offset b_{VV} along the b-direction between neighboring V atoms in a vanadyl chain. (3) Elastic constants of the relaxed-ion stiffness tensor C, Voigt modulus K_R, Reuss modulus K_R. (4) Vibrational contributions at 300 K: zero-point energy (ZPE), vibrational internal energy E_{vib}, vibrational entropy (TS_{vib}), vibrational Helmholtz free energy F_{vib}, total Helmholtz free energy $F= \tilde{E}_{min} + F_{vib}$, and vibrational heat capacity $C_{V,vib}$.

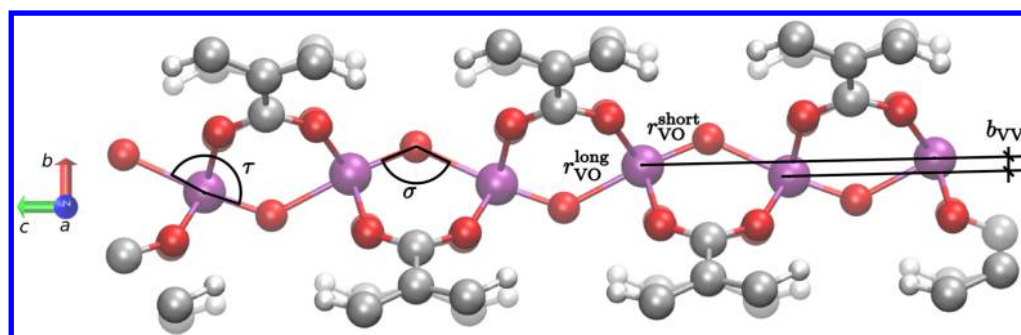**Figure 5.** Definition of structural parameters for Table 5: vanadium−oxide distances r_{VO}^{short} and r_{VO}^{long}, offset b_{VV}, octahedral backbone angle τ, and superexchange angle σ.

Using a fit to the Vinet equation of state (eq 3), the equilibrium volume is found, and calculation of the frequencies shows no imaginary frequencies to be present for this NP structure. Table 5 shows the optimized fitting parameters. A measure for the overall quality of the fit is given by the rmsd in eq 12. Using an uncorrelated uniform noise distribution of ±1 meV, error bars are calculated on all fitting parameters from 10^5 noisy data sets. The equilibrium energy $\tilde{E}_{min}$ and volume V_{min} show only a very small error bar for both the LP and NP structure. The derivative of the bulk modulus B'_0 is most error prone.

The equilibrium volume of the NP structure is 904.8 Å³, about 42% smaller than that of the LP structure. This value is in fairly good agreement with the experimental NP volume of 947 Å³ (for MIL-47(V^{IV})[26] and 908 Å³ for MIL-47(V^{III}).[25] Energetically, i.e., without taking into account temperature effects, the NP structure is only 13.8 meV less stable than the LP structure.

In Table 5, the fitted bulk modulus B_0 roughly halves when going from the LP to the NP form. This may appear strange at first, but is in line with the strongly negative value of the pressure derivative of the bulk modulus B'_0. The latter shows that increasing the pressure on the MIL-47(V) LP structure leads to a significant decrease in its bulk modulus, while decreasing the pressure increases the MIL-47(V)'s resistance to deformation. In the case of the NP structure, B'_0 is much weaker and shows an opposite sign. As such, the resistance to deformation of the NP structure will increase with increasing pressure, i.e., it will be harder to compress the NP structure further.

The structural differences between LP and NP are mainly in the overall unit cell volume and shape with limited internal reorganization. The a and b lattice vectors change significantly, leading to a reduction of the pore opening angle δ from 80° to 39°. The obtained lattice parameters are in good agreement with the experimental values for NP MIL-47(V^{III}) and MIL-47(V^{IV}).[25,26] In addition to the volume change, the symmetry reduces from an orthorhombic cell for the LP structure to a monoclinic cell for the NP structure. Our computed β lattice angle of 112.4° is in good agreement with the experimental values[25,26] of 114° for NP MIL-47(V^{IV}) and 104−115° for NP MIL-47(V^{III}).

In both the LP and NP structures, the VO_6 octahedra are asymmetrically distorted, as was already previously reported for the LP structure.[23,67] The structural parameters describing these distortions are defined in Figure 5. The compressed apex r_{VO}^{short} of the octahedron is indicative of a double bond (V=O). The elongated apex r_{VO}^{long} is indicative of a *trans* bond (V⋯O).[68] The octahedral backbone angle τ (angle O=V⋯O) is expected to be 180° in a perfect octahedron, but it is distorted to 175° for the LP structure and 171° for the NP structure. In contrast, the superexchange angle σ is the angle between subsequent octahedra in the vanadyl chain and remains identical between the LP and NP structures. The distortions in the τ angle and the compressed/elongated vanadium−oxygen distance r_{VO}^{short}/ r_{VO}^{long} results in a zigzag configuration of the vanadiums in a single vanadyl chain. The offset b_{VV} in the *b*-direction between neighboring vanadiums is 0.31 and 0.43 Å for the LP and NP structure, respectively. Such a symmetry breaking in the VO_6 octahedra has previously been shown to be energetically more favorable than a vanadyl chain of perfect octahedra.[23]

5.2. Temperature Effects. Based on the computed phonon frequencies, a rough estimate of temperature effects can be made. This is very interesting for the system at hand because finite temperature contributions to the (Helmholtz) free energy F could shift the relative stability (of only 13.8 meV at 0 K) of the LP and NP structure. This is the case for other breathing MOFs; however, for the MIL-47(V) such thermally induced breathing has not been observed and is thus not expected.

At 0 K, vibrational contributions to the free energy are limited to the zero-point energy (ZPE). As shown in Table 5, the ZPE of the LP and NP structures differs by only 23 meV, and this difference stabilizes the LP structure further in comparison to the NP structure. At 300 K, the vibrational entropic contribution $−TS_{vib}$ to the Helmholtz free energy favors the LP structure significantly (by 136 meV). The LP structure is indeed expected to have more freedom than the compact NP structure. A similar entropic stabilization of the LP was computed for other materials, for instance for the MIL-53(Ga) and MIL-53(Al) materials by Boutin and co-workers.[69] Overall, the total Helmholtz free energy $F = \tilde{E}_{min} + F_{vib}$ of the LP structure is 142 meV more stable than the NP structure at 300 K. Thermal contributions thus stabilize the LP shape, which is in accordance with the LP MIL-47(V) structure being experimentally observed at finite temperature.

The phonon frequency spectrum in Figure 6 is very similar for the LP and NP structure. Frequencies below 400 cm^{-1} show the largest differences (see inset of Figure 6). The lowest nonzero frequency is as low as 18.6 and 13.1 cm^{-1} for the LP and NP, respectively. These and other low-frequency motions describe twisting of the vanadyl chains with respect to each other and similar coherent large-scale motions involving a lot of mass.

Other particularly interesting frequencies are those that describe the linker flexibility. The terephthalate linkers are suspected to be able to rotate as hindered rotors. To investigate their behavior, the partial Hessian vibrational analysis (PHVA) combined with the mobile block Hessian (MBH) approach is employed, i.e., the PHVA/MBH approach as proposed by Ghysels and co-workers.[70] In this combined approach, the terephthalate rings are treated as four mobile blocks that may translate and/or rotate without changing their internal geometry, while the other framework atoms are given an infinite mass such that they remain immobile in the vibrational analysis. This limits the degrees of freedom to only 24
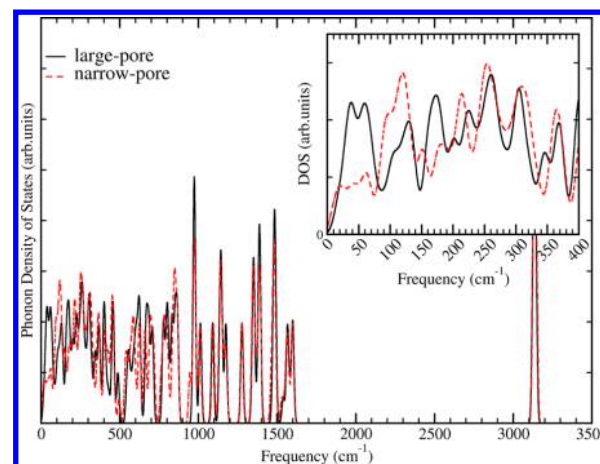

Figure 6. Comparison of the phonon frequency spectrum of the LP (black curves) and the NP (red dashed curves) structures of MIL-47(V). A Gaussian smearing with a standard deviation of 8 cm^{-1} was applied to the computed frequencies. The inset zooms in on the low-frequency region (0−400 cm^{-1}).

frequencies, i.e., six per mobile block. The frequencies are identified to represent linker rotations by computing the variance in dihedral linker angles along the corresponding modes, which is also verified by visualization.

For the LP structure, these linker rotations (wagging) have the four lowest frequencies in the combined PHVA/MBH spectrum and are quasi-degenerate, corresponding to symmetric and asymmetric motions of the four linkers. The degeneracy implies that the individual benzene rotations are motions that couple little with each other. This is in line with the previously noted one-dimensional nature of this material, showing the vanadyl chains to be uncoupled.[23] The linker rotations have a frequency of 42 cm^{-1} (energy 5.2 meV), which is in perfect agreement with the first peak at 5.2 meV in inelastic neutron scattering experiments at 200 K.[34]

The benzene rotation frequencies ω may be linked to force constants by using the principal inertia moments I of benzene. The force constant for the benzene rotation φ is estimated with $I\omega^2$ and is found to be approximately 1.3 kJ/mol/rad^2. For the NP structure, the degeneracy of the linker rotations is broken, giving four different frequencies: 49.0 and 63.3 cm^{-1} for asymmetric rotations of pairs of benzenes and the higher frequencies 116.8, and 125.5 cm^{-1} for symmetric rotations. This is seen in the inset of Figure 6, which shows a suppression of the feature around 40−50 cm^{-1} in favor of a feature around 100 cm^{-1}. The degeneracy is probably broken because of symmetry reduction of the unit cell to a monoclinic structure rather than an orthorhombic structure, in addition to symmetry breaking in the linker orientations of the NP structure. All four frequencies are higher for the NP than for the LP structure, indicating that linker mobility is reduced in the NP structure because of steric hindrance.

6. CONCLUSION

Modeling of flexible materials requires the computation of mechanical properties from first principles, e.g., for screening of materials in a database, for gaining insight into structural transformations, and for force field development. However, this paper shows that computations with periodic density functional theory are challenged by the flexibility of these materials: guidelines from experience with standard solid-state calcu-

lations cannot be simply transferred to flexible porous frameworks.

The MIL-47(V) material has a large-pore and a narrow-pore shape and is used to illustrate the effect of k-point sampling in reciprocal space, symmetry effects, and the effect of Pulay stress. A k-point convergence test should precede any computational study. The k-point set should be sufficiently dense in reciprocal space in each unit cell axis direction. An energy convergence of 1 meV was reached for the MIL-47(V) material with the $2 \times 2 \times 6$ k-point set for the large-pore and $2 \times 6 \times 6$ k-point set for the narrow-pore structure.

Symmetry breaking had to be imposed by manually distorting the structure along its imaginary frequency eigenmodes. MIL-47(V) could successfully lower its energy by distorting the vanadium−oxide distances and angles in the vanadyl chains and by rotating the benzene linkers.

Pulay stress is an artificial stress that tends to lower the volume and is caused by the finite size of the plane wave basis set. During structure optimization, Pulay stress made MIL-47(V) leave its large-pore stable shape to collapse into the narrow-pore shape. As an improved optimization scheme, we propose to optimize subsequently the ion positions and the unit cell shape in a first step. In the next step, an energy-versus-volume profile $E(V)$ should be constructed, in which the energies are computed by fixing the volume at discrete points and optimizing the ions and shape at each chosen volume. An equation of state model can then be fit through the computed energies. Finally, based on this EOS fit, the minimum energy and corresponding volume may be predicted. The volume prediction in this procedure is not affected by Pulay stress.

For the mechanical properties, the bulk modulus was computed in VASP using the harmonic approximation. It is based on numerical differentiation of the ion forces and the stress tensor. The clamped-ion stiffness tensor is corrected with an extra term for the response of the ion positions, to obtain the relaxed-ion stiffness tensor C. The Reuss modulus follows from taking the inverse of C. It describes the resistance of a single crystal to isotropic pressure, and it should in principle be identical to the volume derivative of the pressure, i.e., the curvature of the EOS $E(V)$ curve. However, the harmonic approach can differ from the EOS approach for three reasons: anharmonicity, eggbox effect, and Pulay effects. These errors propagate into the Reuss modulus. Indeed, the a and b axis of MIL-47(V) are strongly coupled when the unit cell deforms, which expresses itself in numerical instability in the inversion of C. The computed MIL-47(V) Reuss modulus is extremely sensitive to these effects. For a flexible material, it is therefore advisable to resort to the EOS fit procedure.

Lastly, the EOS structure optimization procedure has been repeated for the NP structure of MIL-47(V), and mechanical and thermal properties of the LP and NP structure have been compared. The predicted volumes lie fairly close to the experimental values. Energetically, the entropic contribution to the free energy favors the LP phase by 136 meV at 300 K, and overall the LP is computed to be more stable than the NP by 142 meV at 300 K. Symmetry breaking is again necessary to find a stable equilibrium point: the unit cell is monoclinic, degeneracy in linker rotation frequencies is removed, and vanadium−oxide distances are not all equivalent.

In summary, anisotropic flexibility makes a structure optimization of MOF materials a delicate task. We expect that equal caution should be taken for other materials with strong coupling between the lattice vectors, as is here the case

for the a and b direction of MIL-47(V). Symmetry breaking should be allowed in the optimization, and the EOS procedure should be used to avoid the effects of Pulay stress inherent in a finite basis set. Further research may include the accurate characterization of the (free) energy barrier, which is essential in force field development.

■ ASSOCIATED CONTENT

Ⓢ Supporting Information

The Supporting Information is available free of charge on the ACS Publications website at DOI: 10.1021/acs.jpcc.5b06809.

1) Visualization of eggbox effect for the LP structure, 2) k-point convergence of the energy for the NP structure, 3) bulk moduli computed for LP structures with various computational settings, 4) comparison of Vinet EOS to Birch−Murnaghan EOS, 5) parameters obtained from EOS fit, 6) Pulay stress tensor with various computational settings, and 7) Hirshfeld-I charges (PDF)

The LP and NP structure from the EOS optimization procedure with $2 \times 2 \times 6$ and $2 \times 6 \times 6$ k-points, respectively, are available in the database of the Cambridge Crystallographic Data Centre (CCDC 1419980 for LP, CCDC 1419981 for NP).

■ AUTHOR INFORMATION

Corresponding Author

*Phone: +32 9 264 65 63. E-mail: an.ghysels@ugent.be.

Author Contributions

§D.E.P.V. and K.L.: These authors contributed equally.

Notes

The authors declare no competing financial interest.

■ ACKNOWLEDGMENTS

■ REFERENCES

(1) Long, J. R.; Yaghi, O. M. the Pervasive Chemistry of Metal-Organic Frameworks. *Chem. Soc. Rev.* **2009**, *38*, 1213−1214.

(2) Zhang, S.-Y.; Zhang, Z.; Zaworotko, M. J. Topology, Chirality and Interpenetration in Coordination Polymers. *Chem. Commun.* **2013**, *49*, 9700−9703.

(3) Rosseinsky, M. Recent Developments in Metal-Organic Framework Chemistry: Design, Discovery, Permanent Porosity and Flexibility. *Microporous Mesoporous Mater.* **2004**, *73*, 15−30.

(4) Alaerts, L.; Kirschhock, C. E. A.; Maes, M.; van der Veen, M. A.; Finsy, V.; Depla, A.; Martens, J. A.; Baron, G. V.; Jacobs, P. A.; Denayer, J. E. M.; De Vos, D. E. Selective Adsorption and Separation of Xylene Isomers and Ethylbenzene with the Microporous Vanadium(IV) Terephthalate MIL-47. *Angew. Chem., Int. Ed.* **2007**, *46*, 4293−4297.

(5) Rosenbach, N.; Jobic, H.; Ghoufi, A.; Salles, F.; Maurin, G.; Bourrelly, S.; Llewellyn, P. L.; Devic, T.; Serre, C.; Férey, G. Quasi-Elastic Neutron Scattering and Molecular Dynamics Study of Methane Diffusion in Metal Organic Frameworks MIL-47(V) and MIL-53(Cr). *Angew. Chem., Int. Ed.* **2008**, *47*, 6611−5.

(6) Murray, L. J.; Dinca, M.; Long, J. R. Hydrogen Storage in Metal-Organic Frameworks. *Chem. Soc. Rev.* **2009**, *38*, 1294−1314.

(7) Bueno-Pérez, R.; Garcia-Perez, E.; Gutierrez-Sevillano, J. J.; Merkling, P. J.; Calero, S. A Simulation Study of Hydrogen in Metal-Organic Frameworks. *Adsorpt. Sci. Technol.* **2010**, *28*, 823−835. 35th Iberian Meeting on Adsorption, Univ Lisbon, Fac Sci, Lisbon, Portugal, Sep 8−10, 2010.

(8) Gascon, J.; Kapteijn, F. Metal-Organic Framework Membranes-High Potential, Bright Future? *Angew. Chem., Int. Ed.* **2010**, *49*, 1530−1532.

(9) Biswas, S.; Vanpoucke, D. E. P.; Verstraelen, T.; Vandichel, M.; Couck, S.; Leus, K.; Liu, Y.-Y.; Waroquier, M.; Van Speybroeck, V.; Denayer, J. F. M.; Van der Voort, P. New Functionalized Metal-Organic Frameworks MIL-47-X (X = -Cl, -Br, -CH₃, -CF₃, -OH, -OCH₃): Synthesis, Characterization, and CO₂ Adsorption Properties. *J. Phys. Chem. C* **2013**, *117*, 22784−22796.

(10) Llewellyn, P. L.; Bourrelly, S.; Vagner, C.; Heymans, N.; Leclerc, H.; Ghoufi, A.; Bazin, P.; Vimont, A.; Daturi, M.; Devic, T.; Serre, C.; Weireld, G. D.; Maurin, G. Evaluation of MIL-47(V) for CO₂-Related Applications. *J. Phys. Chem. C* **2013**, *117*, 962−970.

(11) Ramsahye, N. A.; Maurin, G.; Bourrelly, S.; Llewellyn, P. L.; Devic, T.; Serre, C.; Loiseau, T.; Férey, G. Adsorption of CO2 in Metal Organic Frameworks of Different Metal Centres: Grand Canonical Monte Carlo Simulations Compared to Experiments. *Adsorption* **2007**, *13*, 461−467.

(12) Yazaydın, A. O.; Snurr, R. Q.; Park, T.-H.; Koh, K.; Liu, J.; LeVan, M. D.; Benin, A. I.; Jakubczak, P.; Lanuza, M.; Galloway, D. B.; Low, J. J.; Willis, R. R. Screening of Metal-Organic Frameworks for Carbon Dioxide Capture from Flue Gas Using a Combined Experimental and Modeling Approach. *J. Am. Chem. Soc.* **2009**, *131*, 18198−18199.

(13) Kolokolov, D. I.; Jobic, H.; Stepanov, A. G.; Ollivier, J.; Rives, S.; Maurin, G.; Devic, T.; Serre, C.; Férey, G. Experimental and Simulation Evidence of a Corkscrew Motion for Benzene in the Metal-Organic Framework MIL-47. *J. Phys. Chem. C* **2012**, *116*, 15093−15098.

(14) Ghysels, A.; Vanduyfhuys, L.; Vandichel, M.; Waroquier, M.; Van Speybroeck, V.; Smit, B. on the Thermodynamics of Framework Breathing: A Free Energy Model for Gas Adsorption in MIL-53. *J. Phys. Chem. C* **2013**, *117*, 11540−11554.

(15) Vanduyfhuys, L.; Verstraelen, T.; Vandichel, M.; Waroquier, M.; Van Speybroeck, V. Ab Initio Parametrized Force Field for the Flexible Metal-Organic Framework MIL-53(Al). *J. Chem. Theory Comput.* **2012**, *8*, 3217−3231.

(16) Stroppa, A.; Jain, P.; Barone, P.; Marsman, M.; Perez-Mato, J. M.; Cheetham, A. K.; Kroto, H. W.; Picozzi, S. Electric Control of Magnetization and Interplay Between Orbital Ordering and Ferroelectricity in a Multiferroic Metal-Organic Framework. *Angew. Chem., Int. Ed.* **2011**, *50*, 5847−5850.

(17) Combelles, C.; Yahia, M. B.; Pedesseau, L.; Doublet, M.-L. Fe^II/Fe^III Mixed-Valence State Induced by Li-Insertion into the Metal-Organic-Framework Mil53(Fe): A DFT+U Study. *J. Power Sources* **2011**, *196*, 3426−3432.

(18) Sillar, K.; Sauer, J. Ab Initio Prediction of Adsorption Isotherms for Small Molecules in Metal-Organic Frameworks: The Effect of Lateral Interactions for Methane/CPO-27-Mg. *J. Am. Chem. Soc.* **2012**, *134*, 18354−18365.

(19) Flage-Larsen, E.; Røyset, A.; Cavka, J. H.; Thorshaug, K. Band Gap Modulations in UiO Metal-Organic Frameworks. *J. Phys. Chem. C* **2013**, *117*, 20610−20616.

(20) Wang, Z.; Jain, P.; Choi, K.-Y.; van Tol, J.; Cheetham, A. K.; Kroto, H. W.; Koo, H.-J.; Zhou, H.; Hwang, J.; Choi, E. S.; Whangbo, M.-H.; Dalal, N. S. Dimethylammonium Copper Formate [(CH₃)₂NH₂]Cu(HCOO)₃: A Metal-Organic Framework with Quasi-One-Dimensional Antiferromagnetism and Magnetostriction. *Phys. Rev. B: Condens. Matter Mater. Phys.* **2013**, *87*, 224406.

(21) Chen, X.; Wang, Y.-Y.; Liu, B.; Yin, B.; Liu, P.; Shi, Q.-Z. New Two-Dimensional Mn(II) Metal-Organic Framework Featured Spin Canting. *Dalton Trans.* **2013**, *42*, 7092−7100.

(22) Flage-Larsen, E.; Thorshaug, K. Linker Conformation Effects on the Band Gap in Metal-Organic Frameworks. *Inorg. Chem.* **2014**, *53*, 2569−2572.

(23) Vanpoucke, D. E. P.; Jaeken, J. W.; Baerdemacker, S. D.; Lejaeghere, K.; Van Speybroeck, V. Quasi-1D Physics in Metal-Organic Frameworks: MIL-47(V) from First Principles. *Beilstein J. Nanotechnol.* **2014**, *5*, 1738−1748.

(24) Serre, C.; Bourrelly, S.; Vimont, A.; Ramsahye, N. A.; Maurin, G.; Llewellyn, P. L.; Daturi, M.; Filinchuk, Y.; Leynaud, O.; Barnes, P.; Férey, G. an Explanation for the Very Large Breathing Effect of a Metal-Organic Framework During CO₂ Adsorption. *Adv. Mater.* **2007**, *19*, 2246−2251.

(25) Leclerc, H.; Devic, T.; Devautour-Vinot, S.; Bazin, P.; Audebrand, N.; Férey, G.; Daturi, M.; Vimont, A.; Clet, G. Influence of the Oxidation State of the Metal Center on the Flexibility and Adsorption Properties of a Porous Metal Organic Framework: MIL-47(V). *J. Phys. Chem. C* **2011**, *115*, 19828−19840.

(26) Yot, P. G.; Ma, Q.; Haines, J.; Yang, Q.; Ghoufi, A.; Devic, T.; Serre, C.; Dmitriev, V.; Ferey, G.; Zhong, C.; Maurin, G. Large Breathing of the MOF MIL-47(V^IV) Under Mechanical Pressure: A Joint Experimental-Modelling Exploration. *Chem. Sci.* **2012**, *3*, 1100−1104.

(27) Alhamami, M.; Doan, H.; Cheng, C.-H. A Review on Breathing Behaviors of Metal-Organic-Frameworks (MOFs) for Gas Adsorption. *Materials* **2014**, *7*, 3198−3250.

(28) Lejaeghere, K.; Van Speybroeck, V.; Van Oost, G.; Cottenier, S. Error Estimates for Solid-State Density-Functional Theory Predictions: An Overview by Means of the Ground-State Elemental Crystals. *Crit. Rev. Solid State Mater. Sci.* **2014**, *39*, 1−24.

(29) Tan, J. C.; Civalleri, B.; Lin, C. C.; Valenzano, L.; Galvelis, R.; Chen, P. F.; Bennett, T. D.; Mellot-Draznieks, C.; Zicovich-Wilson, C. M.; Cheetham, A. K. Exceptionally Low Shear Modulus in a Prototypical Imidazole-Based Metal-Organic Framework Material. *Phys. Rev. Lett.* **2012**, *108*, 095502.

(30) Walker, A. M.; Civalleri, B.; Slater, B.; Mellot-Draznieks, C.; Corà, F.; Zicovich-Wilson, C. M.; Román-Pérez, G.; Soler, J. M.; Gale, J. D. Flexibility in a Metal-Organic Framework Material Controlled by Weak Dispersion Forces: The Bistability of MIL-53(Al). *Angew. Chem., Int. Ed.* **2010**, *49*, 7501−7503.

(31) Coudert, F. X.; Mellot-Draznieks, C.; Fuchs, A. H.; Boutin, A. Double Structural Transition in Hybrid Material MIL-53 upon Hydrocarbon Adsorption: The Thermodynamics Behind the Scenes. *J. Am. Chem. Soc.* **2009**, *131*, 3442−3443.

(32) Coudert, F. X.; Mellot-Draznieks, C.; Fuchs, A. H.; Boutin, A. Prediction of Breathing and Gate-Opening Transitions upon Binary Mixture Adsorption in Metal-Organic Frameworks. *J. Am. Chem. Soc.* **2009**, *131*, 11329−11332.

(33) Neimark, A. V.; Coudert, F.; Boutin, A.; Fuchs, A. H. Stress-Based Model for the Breathing of Metal-Organic Frameworks. *J. Phys. Chem. Lett.* **2010**, *1*, 445−449.

(34) Kolokolov, D.; Jobic, H.; Stepanov, A.; Plazanet, M.; Zbiri, M.; Ollivier, J.; Guillerm, V.; Devic, T.; Serre, C.; Férey, G. Comparison of the Dynamics of MIL-53(Cr) and MIL-47(V) Frameworks Using Neutron Scattering and DFT Methods. *Eur. Phys. J.: Spec. Top.* **2010**, *189*, 263−271.

(35) Hendon, C. H.; Tiana, D.; Fontecave, M.; Sanchez, C.; D'arras, L.; Sassoye, C.; Rozes, L.; Mellot-Draznieks, C.; Walsh, A. Engineering the Optical Response of the Titanium-MIL-125 Metal-Organic Framework Through Ligand Functionalization. *J. Am. Chem. Soc.* **2013**, *135*, 10942−10945.

(36) Liu, Y.; Her, J. H.; Dailly, A.; Ramirez-Cuesta, A. J.; Neumann, D.; Brown, C. M. Reversible Structural Transition in MIL-53 with Large Temperature Hysteresis. *J. Am. Chem. Soc.* **2008**, *130*, 11813−11818.

(37) Ortiz, A. U.; Boutin, A.; Fuchs, A. H.; Coudert, F. Anisotropic Elastic Properties of Flexible Metal-Organic Frameworks: How Soft Are Soft Porous Crystals? *Phys. Rev. Lett.* **2012**, *109*, 195502.

(38) Piccini, G.; Sauer, J. Quantum Chemical Free Energies: Structure Optimization and Vibrational Frequencies in Normal Modes. *J. Chem. Theory Comput.* **2013**, *9*, 5038–5045.

(39) Barthelet, K.; Marrot, J.; Riou, D.; Férey, G. A Breathing Hybrid Organic - Inorganic Solid with Very Large Pores and High Magnetic Characteristics. *Angew. Chem., Int. Ed.* **2002**, *41*, 281.

(40) Wang, X.; Liu, L.; Jacobson, A. J. Intercalation of Organic Molecules into Vanadium(IV) Benzenedicarboxylate: Adsorbate Structure and Selective Absorption of Organosulfur Compounds. *Angew. Chem., Int. Ed.* **2006**, *45*, 6499–6503.

(41) Wang, X.; Eckert, J.; Liu, L.; Jacobson, A. J. Breathing and Twisting: An Investigation of Framework Deformation and Guest Packing in Single Crystals of a Microporous Vanadium Benzenedicarboxylate. *Inorg. Chem.* **2011**, *50*, 2028–2036.

(42) Monkhorst, H. J.; Pack, J. D. Special Points for Brillouin-Zone Integrations. *Phys. Rev. B* **1976**, *13*, 5188–5192.

(43) Froyen, S.; Cohen, M. L. Structural Properties of NaCl and KCl Under Pressure. *J. Phys. C: Solid State Phys.* **1986**, *19*, 2623–2632.

(44) Gomes Dacosta, P.; Nielsen, O. H.; Kunc, K. Stress Theorem in the Determination of Static Equilibrium by the Density Functional Method. *J. Phys. C: Solid State Phys.* **1986**, *19*, 3163–3172.

(45) Vanderbilt, D. Absence of Large Compressive Stress on Si(111). *Phys. Rev. Lett.* **1987**, *59*, 1456–1459.

(46) Francis, G. P.; Payne, M. C. Finite Basis Set Corrections to Total Energy Pseudopotential Calculations. *J. Phys.: Condens. Matter* **1990**, *2*, 4395–4404.

(47) Birch, F. Finite Elastic Strain of Cubic Crystals. *Phys. Rev.* **1947**, *71*, 809–824.

(48) Vinet, P.; Ferrante, J.; Rose, J. H.; Smith, J. R. Compressibility of Solids. *J. Geophys. Res.* **1987**, *92*, 9319–9325.

(49) Hama, J.; Suito, K. The Search for a Universal Equation of State Correct up to Very High Pressures. *J. Phys.: Condens. Matter* **1996**, *8*, 67–81.

(50) Rose, J. H.; Ferrante, J.; Smith, J. R. Universal Binding Energy Curves for Metals and Bimetallic Interfaces. *Phys. Rev. Lett.* **1981**, *47*, 675–678.

(51) Cui, Q.; Bahar, I. *Normal Mode Analysis: Theory and Applications to Biological and Chemical Systems*; Chapman and Hall/CRC: Boca Raton, FL, 2006.

(52) McQuarrie, D. A.; Simon, J. D. *Physical Chemistry: A Molecular Approach*; University Science Books: Sausalito, CA, 1997.

(53) Wu, X.; Vanderbilt, D.; Hamann, D. R. Systematic Treatment of Displacements, Strains, and Electric Fields in Density-Functional Perturbation Theory. *Phys. Rev. B: Condens. Matter Mater. Phys.* **2005**, *72*, 035105.

(54) Woodcock, H. L.; Zheng, W. J.; Ghysels, A.; Shao, Y. H.; Kong, J.; Brooks, B. R. Vibrational Subsystem Analysis: A Method for Probing Free Energies and Correlations in the Harmonic Limit. *J. Chem. Phys.* **2008**, *129*, 214109.

(55) Ghysels, A.; Van Speybroeck, V.; Pauwels, E.; Catak, S.; Brooks, B. R.; Van Neck, D.; Waroquier, M. Comparative Study of Various Normal Mode Analysis Techniques Based on Partial Hessians. *J. Comput. Chem.* **2010**, *31*, 994–1007.

(56) Ghysels, A.; Miller, B. T.; Pickard, F. C.; Brooks, B. R. Comparing Normal Modes Across Different Models and Scales: Hessian Reduction Versus Coarse-Graining. *J. Comput. Chem.* **2012**, *33*, 2250–2275.

(57) Ortiz, A. U.; Boutin, A.; Fuchs, A. H.; Coudert, F. X. Metalorganic Frameworks with Wine-Rack Motif: What Determines Their Flexibility and Elastic Properties? *J. Chem. Phys.* **2013**, *138*, 174703.

(58) Marmier, A.; Lethbridge, Z. A. D.; Walton, R. I.; Smith, C. W.; Parker, S. C.; Evans, K. E. ElAM: a Computer Program for the Analysis and Representation of Anisotropic Elastic Properties. *Comput. Phys. Commun.* **2010**, *181*, 2102–2115.

(59) Allen, F. H. The Cambridge Structural Database: A Quarter of a Million Crystal Structures and Rising. *Acta Crystallogr., Sect. B: Struct. Sci.* **2002**, *B58*, 380–388.

(60) Perdew, J. P.; Burke, K.; Ernzerhof, M. Generalized Gradient Approximation Made Simple. *Phys. Rev. Lett.* **1996**, *77*, 3865–3868.

(61) Csonka, G.; Perdew, J.; Ruzsinszky, A.; Philipsen, P.; Lebègue, S.; Paier, J.; Vydrov, O.; Ángyán, J. Assessing the Performance of Recent Density Functionals for Bulk Solids. *Phys. Rev. B: Condens. Matter Mater. Phys.* **2009**, *79*, 155107.

(62) Haigis, V.; Belkhodja, Y.; Coudert, F.-X.; Vuilleumier, R.; Boutin, A. Challenges in First-Principles NPT Molecular Dynamics of Soft Porous Crystals: A Case Study on MIL-53(Ga). *J. Chem. Phys.* **2014**, *141*, 064703.

(63) Grimme, S.; Antony, J.; Ehrlich, S.; Krieg, H. A Consistent and Accurate Ab Initio Parametrization of Density Functional Dispersion Correction (DFT-D) for the 94 Elements H-Pu. *J. Chem. Phys.* **2010**, *132*, 154104.

(64) Grimme, S.; Ehrlich, S.; Goerigk, L. Effect of the Damping Function in Dispersion Corrected Density Functional Theory. *J. Comput. Chem.* **2011**, *32*, 1456–1465.

(65) Vanduyfhuys, L.; Ghysels, A.; Rogge, S.; Demuynck, R.; Van Speybroeck, V. Semi-Analytical Mean-Field Model for Predicting Breathing in Metal-Organic Frameworks. *Mol. Simul.* **2015**, *41*, 1311.

(66) Becke, A. D. Density-Functional Thermochemistry. III. The Role of Exact Exchange. *J. Chem. Phys.* **1993**, *98*, 5648.

(67) Meilikhov, M.; Yusenko, K.; Torrisi, A.; Jee, B.; Mellot-Draznieks, C.; Pöppl, A.; Fischer, R. A. Reduction of a Metal-Organic Framework by an Organometallic Complex: Magnetic Properties and Structure of the Inclusion Compound $[(\eta^5\text{-}C_5H_5)_2Co]_{0.5}$@MIL-47(V). *Angew. Chem., Int. Ed.* **2010**, *49*, 6212–6215.

(68) Weeks, C.; Song, Y.; Suzuki, M.; Chernova, N. A.; Zavalij, P. Y.; Whittingham, M. S. The One Dimensional Chain Structures of Vanadyl Glycolate and Vanadyl Acetate. *J. Mater. Chem.* **2003**, *13*, 1420–1423.

(69) Coudert, F. X.; Ortiz, A. U.; Haigis, V.; Bousquet, D.; Fuchs, A. H.; Ballandras, A.; Weber, G.; Bezverkhyy, I.; Geoffroy, N.; Bellat, J.; Ortiz, G.; Chaplais, J.; Patarin, J.; Boutin, A. Water Adsorption in Flexible Gallium-Based MIL-53 MetalOrganic Framework. *J. Phys. Chem. C* **2014**, *118*, 5397–5405.

(70) de Moor, B. A.; Ghysels, A.; Reyniers, M. F.; van Speybroeck, V.; Waroquier, M.; Marin, G. B. Normal Mode Analysis in Zeolites: Toward an Efficient Calculation of Adsorption Entropies. *J. Chem. Theory Comput.* **2011**, *7*, 1090–1101.